THE JOURNAL OF PHYSICAL CHEMISTRY C

Article

Cite This: J. Phys. Chem. C XXXX, XXX, XXX−XXX

pubs.acs.org/JPCC

In Situ Formation of TiB_2 Nanoparticles for Enhanced Dehydrogenation/Hydrogenation Reaction Kinetics of $LiBH_4$−MgH_2 as a Reversible Solid-State Hydrogen Storage Composite System

Fahim Karimi,*[,†] María V. C. Riglos,[‡] Antonio Santoru,[†] Armin Hoell,[∥] Vikram S. Raghuwanshi,[∥] Chiara Milanese,[⊥] Nils Bergemann,[†] Claudio Pistidda,[†] Pau Nolis,[#] Maria D. Baro,[▽] Gökhan Gizer,[†] Thi-Thu Le,[†] P. Klaus Pranzas,[†] Martin Dornheim,[†] Thomas Klassen,[†] Andreas Schreyer,[○] and Julián Puszkiel[†,§]

[†]Department of Nanotechnology, Institute of Materials Research, Helmholtz−Zentrum Geesthacht, Max-Planck-Straße 1, 21502 Geesthacht, Germany

[‡]Department of Metalphysics and [§]Department of Physicochemistry of Materials, Consejo Nacional de Investigaciones Científicas y Técnicas (CONICET) y Centro Atómico Bariloche, Av. Bustillo km 9500, R8402AGP S.C. de Bariloche, Argentina

[∥]Institut für Nanospektroskopie, Helmholtz-Zentrum Berlin für Materialien und Energie, Hahn-Meitner-Platz 1, 14109 Berlin, Germany

[⊥]Pavia Hydrogen Lab, C.S.G.I. and Chemistry Department, Physical Chemistry Section, University of Pavia, Viale Taramelli, 16, 27100 Pavia, Italy

[#]Servei de Ressonància Magnètica Nuclear and [▽]Departament de Física, Facultat de Ciències, Universitat Autònoma de Barcelona, E-08193 Cerdanyola del Vallès, Barcelona, Spain

[○]European Spallation Source ERIC, P.O. Box 176, S-22100 Lund, Sweden

Supporting Information

ABSTRACT: To enhance the dehydrogenation/rehydrogenation kinetic behavior of the $LiBH_4$−MgH_2 composite system, TiF_4 is used as an additive. The effect of this additive on the hydride composite system has been studied by means of laboratory and advanced synchrotron techniques. Investigations on the synthesis and mechanism upon hydrogen interaction show that the addition of TiF_4 to the $LiBH_4$−MgH_2 composite system during the milling procedure leads to the in situ formation of well-distributed nanosized TiB_2 particles. These TiB_2 nanoparticles act as nucleation agents for the formation of MgB_2 upon dehydrogenation process of the hydride composite system. The effect of TiB_2 nanoparticles is maintained upon cycling.

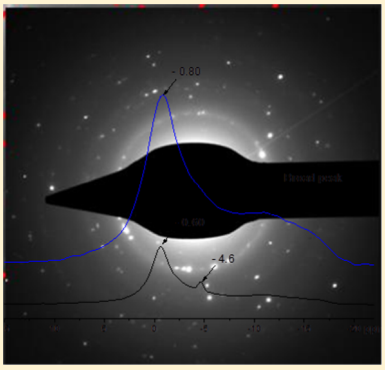

INTRODUCTION

Complex metal hydrides are considered as potential candidates for hydrogen storage.[1,2] They provide an efficient and safe way to store hydrogen in mobile applications in comparison to hydrogen stored in gaseous or liquid state.[3] Among all complex hydrides, $LiBH_4$ has been widely investigated in the past decade.[4−22] This is due to its high gravimetric and volumetric hydrogen storage capacities, i.e., 18.4 wt % and 121 kg/m^3, respectively.[23] Nonetheless, the thermodynamic stability of $LiBH_4$ precludes the reversible reaction with hydrogen at moderate temperatures and pressures.[24] $LiBH_4$ releases hydrogen above its melting point (275 °C)[25] at temperatures between 480 and 490 °C through the reaction (1): $LiBH_4 \rightarrow B + LiH + 1.5H_2$ (ΔH = 94 kJ/mol H_2) and its rehydrogenation occurs only above 650 °C and 150 bar of hydrogen pressure.[4,5,22] Furthermore, highly toxic borane compounds can be formed during the dehydrogenation process of $LiBH_4$.[18] Many attempts were taken to face the poor reversibility and sluggish rehydrogenation kinetic of this system.[18−21] A breakthrough was achieved using the concept of reactive hydride composite (RHC).[26,27] In this approach, a highly stable complex hydride such as $LiBH_4$ is mixed with a less stable binary hydride like MgH_2 (74 kJ/mol H_2) to reduce the overall thermodynamic stability of the composite system.[26−39] The stoichiometric hydride composite system $2LiBH_4 + MgH_2$ (Li-RHC) has a theoretical gravimetric capacity of 11.5 wt % and a theoretical reaction enthalpy of 45.9 kJ/mol H_2, based on reaction (2): $2LiBH_4 + MgH_2 \leftrightarrows 2LiH + MgB_2 + 4H_2$. Thus,

Received: March 7, 2018
Revised: May 5, 2018
Published: May 9, 2018

DOI: 10.1021/acs.jpcc.8b02258
J. Phys. Chem. C XXXX, XXX, XXX−XXX

the overall thermodynamic stability of this system is reduced in comparison to reaction (1). This is mainly due to the exothermal formation of MgB_2 during the desorption process. Therefore, the formation of MgB_2 is the driving force for stabilizing the decomposition products of $LiBH_4$. Experimentally, however, the dehydrogenation reaction of the Li-RHC system does not occur according to reaction (2). It rather decomposes in two reaction steps according to the following reaction (3): $2LiBH_4 + MgH_2 \rightarrow Mg + 2LiBH_4 + H_2 \rightarrow 2LiH + MgB_2 + 4H_2$.[28] Furthermore, this reaction only occurs at hydrogen backpressures higher than 3 bar and 400 °C. At hydrogen backpressures lower than 3 bar, this composite system decomposes independently, and MgB_2 is not formed.[40,41] In recent years, notable improvements in the dehydrogenation/hydrogenation kinetic behavior of RHCs have been achieved by the addition of transition metals halides.[42−52]

In this work, the effect of TiF_4 as an additive in the Li-RHC is investigated. The addition of TiF_4 in the Li-RHC is motivated by the fact that titanium and fluorine have one of the lowest atomic masses among transition metals and halides, respectively, which leads to a small loss in gravimetric hydrogen storage capacity of the composite system. Systematic, and extensive experimental investigations were conducted in this work by the use of laboratory and advanced synchrotron techniques to shed some light on the reasons hidden behind the catalytic effect of TiF_4 in the Li-RHC system.

The results obtained in this work contribute to the fundamental understanding of the mechanism of nanosized transition metal borides and their effects on the hydride composite systems.

EXPERIMENTAL SECTION

$LiBH_4$ powder (purity >90%), MgH_2 (purity >95%), and titanium fluoride (TiF_4, purity >99.9%) were purchased from Alfa Aesar company and used as starting materials. $2LiBH_4 + MgH_2$ mixtures were prepared with and without additive (TiF_4) by high energy ball milling in a SPEX 8000 mixer mill using a stainless steel vial and balls, respectively. The ball-to-powder ratio was chosen to be 10:1. In the first step, MgH_2 was premilled for 5 h. Subsequently, it was mixed with $2LiBH_4$ or $2LiBH_4 + 0.1TiF_4$, and the mixture was further milled for additional 5 h. After milling, $2LiBH_4 + MgH_2 + 0.1TiF_4$ material was subjected to a gas phase analysis. For this, a Hiden Analytical HAL 201 Mass-Spectrometer was used.

Hydrogen kinetic behaviors of the pure and doped sample were assessed in a commercial Sievert's type apparatus (PCTpro 2000). The parameters for volumetric measurements were set to 390 °C at 4 bar H_2 for desorption and 350 °C at 50 bar H_2 for absorption. First, the materials in hydrogenated state were nonisothermally dehydrogenated with a temperature ramp set to 3 °C/min and then two hydrogenation/dehydrogenation cycles in isothermal conditions were preformed. Coupled calorimetric−volumetric measurements of $2LiBH_4 + MgH_2 + 0.1TiF_4$ composite system were performed by connecting a PCT-Pro instrument with a Sensys high-pressure differential scanning calorimeter (Setaram, HP-DSC, France). The experimental parameters were heating ramp at 3 °C/min, backpressure of 4 bar H_2, and final temperature of about 500 °C.

Ex situ laboratory X-ray diffraction (XRD) were collected with a Bruker D8 Advance diffractometer in the Bragg−Brentano geometry using a General Area detector and a Cu X-ray source. The sample was investigated using an airtight sample holder from Bruker. The incoherent scattering of the poly(methyl methacrylate) dome is responsible for the bump observed at low angles in all the diffractograms.

In situ synchrotron radiation X-ray powder diffraction (in situ SR-XPD) measurements were conducted at the powder diffraction beamline D3 at HASYLAB (in DESY, Hamburg, Germany). Sample preparation was carried out in a glovebox under inert conditions. A small amount of sample was charged in a single crystal sapphire capillary. The capillary, subsequently, was mounted in a high-pressure cell and exposed to a monochromatic synchrotron beam. The wavelength of the incident photons was set to about 0.5 Å. The sample was heated up by a tungsten wire under the capillary, whereas the sample temperature was measured by a thermocouple and controlled with a proportional−integral−derivative regulator. The diffracted intensities were collected by using a MarCCD-165 area detector. The acquired two-dimensional patterns were further processed and integrated to one-dimensional (1D) patterns using the program Fit2D.[53]

Anomalous small-angle scattering (ASAXS) measurements were acquired at the 7T-MPW beamline at the synchrotron radiation facility BESSY II (HZB, Berlin, Germany).[54] The beamline was equipped with a Si_{111} double-crystal monochromator and a pair of retractable collimating/focusing mirrors optics, leading to a resolution of $\Delta E/E \sim 2 \times 10^{-4}$. A multiwire proportional counter gas detector (20×20 cm^2, in size) was used to record the scattering data. All the samples were put into circular holes (5 mm in diameter) of a molybdenum holder and sealed with Kapton tape to avoid any oxidation. Two sample-to-detector distances (D_{min} = 780 mm and D_{max} = 3800 mm) were chosen to cover the maximum experimentally accessible scattering vector (q) range. To separate the resonant scattering of Ti-containing nanostructures, all the measurements were carried out close to the K absorption edge of titanium (4966 eV).[55] All the selected energies with their corresponding anomalous dispersion factors are listed in Table 1.[56]

Table 1. Selected Energies for ASAXS Measurements at Titanium K-Edge (4966 eV) and the Corresponding Anomalous Dispersion Coefficients

element	energy (eV)	f'	f''
E1	4600	−2.427	0.508
E2	4905	−4.214	0.454
E3	4955	−6.059	0.462
E4	4964	−7.798	0.587

The raw data were processed using the software provided at the beamline. All the SAXS measurements were integrated and then corrected for detector sensitivity and transmission. Measured intensities were then subtracted by dark current and background. For each measurement, a glassy carbon (with a thickness of 90 μm) and a silver-behenate foil was measured to put the scattering intensities onto absolute scale and to calibrate the q-axis, respectively. Furthermore, energy-dependent inelastic scattering[57] at high q-values were subtracted by following the Porod law. The resonant scattering of Ti-containing structures was separated using the method of Goerigk et al.[58]

The X-ray absorption spectroscopy (XAS) data were collected at the beamline A1 at HASYLAB (DESY, Hamburg,

DOI: 10.1021/acs.jpcc.8b02258
J. Phys. Chem. C XXXX, XXX, XXX−XXX

Germany). The samples were mixed with cellulose (~50 mg) in a mortar and mechanically pressed (with 5 bar) into pellets 10 mm in size. These pellets were fixed in a circular hole of an aluminum sample holder and sealed with Kapton tapes (55 μm, in thickness) to avoid any oxidation of the samples. All the XAS measurements were collected simultaneously in transmission and in fluorescence mode, respectively. The XAS data processing and analysis were carried out by using "IFEFFIT" software package.[59]

The transmission electron microscopy (TEM) characterization was performed in FEI TECNAI G^2 machine using 200 kV, point resolution: 0.12 nm and field emission gun. Dark field (DF) imaging technique was used to distinguish different phases by their diffraction. MgB_2 particles were highlighted by selecting one or more of the following MgB_2 phase's intense reflections (*hkl*) planes: (101), having $|g| = 4.7\ nm^{-1}$, (002), having $|g| = 5.68\ nm^{-1}$, and (110), having $|g| = 6.49\ nm^{-1}$. In the case of the additive (TiF_4), the DF images were obtained by selecting the intense reflections from the following plane families: $(101)_{TiB_2}$, having $|g| = 4.9\ nm^{-1}$, $(002)_{TiB_2}$, having $|g| = 6.19\ nm^{-1}$. Size measurements on every particle were performed by means of an interpolated polygon tool from iTEM software[60] and the values that took into account were those from mean diameter measurements. High-resolution transmission electron microscopy (HR-TEM) images were obtained with a magnification higher than $M > 300k\times$. In HR-TEM images, fast Fourier transform was performed by Digital Micrograph software[61] to obtain the diffraction patterns. Then, the experimental diffraction patterns were compared with the simulated ones obtained by JEMS software..[62] Samples for TEM were prepared by dispersing a small amount of powder in hexane and then ultrasonicating the suspension during 10 min. A drop of this suspension was deposited over a commercial copper grid for TEM coated with a Formvar support film. The samples were exposed to air during a short time.

^{11}B solid-state NMR measurements were carried out on a Bruker Avance 400 MHz spectrometer with a wide bore 9.4 T magnet and employing a boron-free Bruker 4 mm CPMAS probe. The spectral frequency was 128.33 MHz for the ^{11}B nucleus, and the NMR shifts are reported in parts per million (ppm) externally referenced to BF_3Et_2O. The powder materials were packed into 4 mm ZrO_2 rotors in an argon-filled glovebox and sealed with tight-fitting Kel-F caps. The one-dimensional (1D) ^{11}B {1H} magic-angle spinning (MAS) NMR spectra were acquired after a 2.7 μs single $\pi/2$ pulse (corresponding to a radio field strength of 92.6 kHz) and with application of a strong ^1H signal decoupling by using the two-pulse phase modulation scheme. The spectra were recorded at a MAS spinning rate of 12 kHz. Sample spinning was performed using dry nitrogen gas. The recovery delay was set to 10 s. Spectra were acquired at 20 °C (controlled by a Bruker BCU unit).

All sample preparation and handling were carried out in a glovebox under continuously purified argon atmosphere (H_2O and O_2 levels were kept below 10 ppm).

To determine the nature of the Ti-containing species, thermodynamic calculations have been carried out using the HSC Chemistry software version 9.4.1.[63] The calculations have been done based on the reactivity of $2LiBH_4 + MgH_2$ with TiF_4 under different temperature and pressure conditions. The most favorable reactions have been identified through a combination of Gibbs minimization equilibrium with selected solid and gas species. The obtained results represent the ideal phase equilibrium compositions useful to predict the possible reaction mechanisms between the Li-RHC matrix and the additive involving solid products and gaseous species such as B_2H_6, B_xH_y ($x = 5-12$, $y = 5-14$), and fluoride species. For all the calculations, the solid orthorhombic $LiBH_4$ (*Pnma*) is taken into account. $Li_2B_{12}H_{12}$ was not taken into account due to the lack of available physicochemical data.

RESULTS

Volumetric and Calorimetric Measurements: Reaction Kinetic and Reaction Mechanism. The nonisothermal volumetric measurements of pristine $2LiBH_4 + MgH_2$ and $2LiBH_4 + MgH_2 + 0.1TiF_4$ samples are presented in Figure 1.

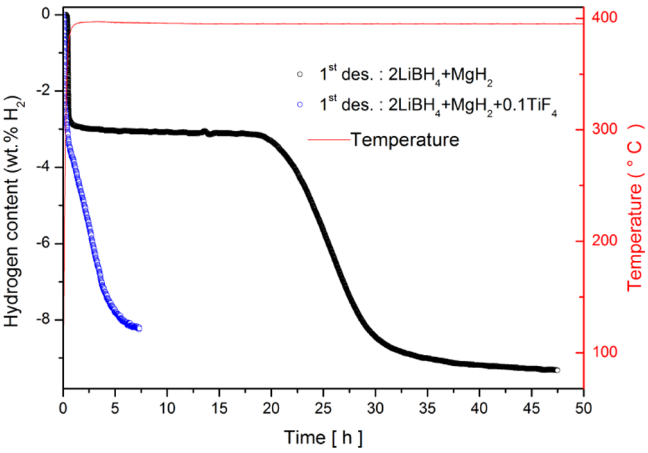

Figure 1. First nonisothermal dehydrogenation reaction from room temperature (RT) to 400 °C, heating rate 3 °C/min, and under PH_2 = 4 bar H_2 dehydrogenation for $2LiBH_4 + MgH_2$ and $2LiBH_4 + MgH_2 + 0.1TiF_4$ hydride systems.

The dehydrogenation reaction of pristine $2LiBH_4 + MgH_2$ (Figure 1) evolves roughly in 20 h. The reaction proceeds in two steps separated by a plateau phase where hydrogen is almost not released. Subsequently, the plateau phase extends the total reaction time by roughly 6.5 h. The second step of the reaction ends the plateau phase, and it is completed after roughly 12 h. The dehydrogenation processes of $2LiBH_4 + MgH_2 + 0.1TiF_4$ (Figure 1) also shows two reaction steps. However, no plateau phase is observed and the overall reaction is completed after roughly 4 h. By adding 10 mol % of TiF_4, the kinetic behavior of the first dehydrogenation is improved by a factor of ~5 in comparison with the pure hydride system. Coupled calorimetric–volumetric measurements during the first dehydrogenation of $2LiBH_4 + MgH_2 + 0.1TiF_4$ (Figure S1, Supporting Information) show that from 50 °C to about 360 °C, the material does not release hydrogen. However, the phase transition of $LiBH_4$ from orthorhombic to hexagonal structure, as well as the melting of the hexagonal structure, is seen in the calorimetric signal at about 120 and 270 °C, respectively.[25,64] Neither the structural phase transition nor the melting point of $LiBH_4$ is affected by the presence of the used additive. The coupled calorimetric–volumetric measurements exhibit the same behavior as the volumetric measurement for $2LiBH_4 + MgH_2 + 0.1TiF_4$ material (Figures S1 and1).

Furthermore, both materials were cycled twice and the results of the second cycle are shown in Figure 2A,B. These volumetric measurements exhibit proper reversibility of $2LiBH_4 + MgH_2 + 0.1TiF_4$ system and still reduced hydrogenation (~1

DOI: 10.1021/acs.jpcc.8b02258
J. Phys. Chem. C XXXX, XXX, XXX–XXX

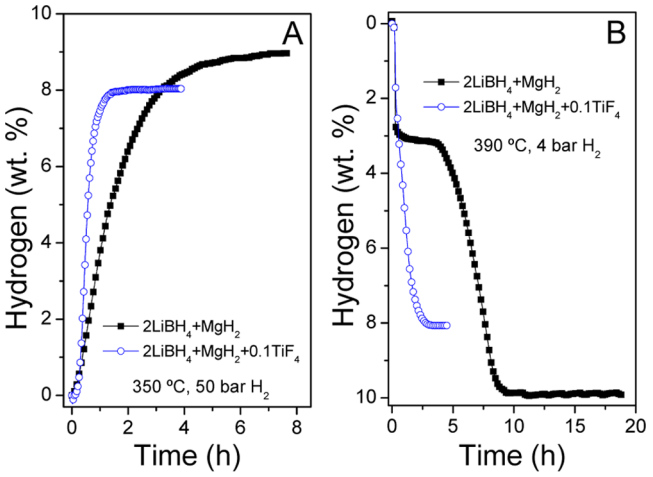

Figure 2. (A) Second hydrogenation and (B) second dehydrogenation for $2LiBH_4 + MgH_2$ and $2LiBH_4 + MgH_2 + 0.1TiF_4$ hydride systems. Isothermal hydrogenation/dehydrogenation at 350 °C under 50 bar H_2 and 390 °C under 4 bar H_2, respectively.

h) and dehydrogenation (~2 h) times. Moreover, the hydrogen capacity remains constant at about 8 wt %, which is lower than the corresponding value of the pristine material. This can be due to a possible interaction between the hydride matrix ($2LiBH_4 + MgH_2$) and the TiF_4 additive.

In Situ SR-XPD Measurements: Phase Transformation and Reaction Paths of Li-RHC. By means of in situ SR-XPD, reaction paths of crystalline phases of $2LiBH_4 + MgH_2 + 0.1TiF_4$ were investigated (Figure 3). The starting material at room temperature consists of $LiBH_4$, MgH_2, and LiF. By increasing the sample temperature, the diffraction peaks of the starting material become sharper and are shifted simultaneously toward the lower diffraction angles. These changes are due to recrystallization of the disordered milled material and enlarging of the respective unit cells owing to the increased temperature at the same time. At around 120 °C, the phase transformation of $LiBH_4$ (from orthorhombic *o*-$LiBH_4$ to hexagonal *h*-$LiBH_4$) is observed. At 280 °C, the diffraction peaks of $LiBH_4$ suddenly diminish due to the melting of $LiBH_4$.[66,67] These findings are in good agreement with the results obtained by coupled calorimetric−volumetric measurements of the first dehydrogenation of the doped system. During the first reaction step, MgH_2 decomposes around 360 °C by forming metallic Mg. In the second reaction step, at roughly 390 °C, the diffraction peaks of Mg decrease, whereas diffraction peaks of MgB_2 phase start to appear. This indicates a mutual reaction between metallic Mg and liquid $LiBH_4$. After dwelling for 30 min at 400 °C (Figure S2, Supporting Information), LiF phase and small amount of MgO phase are observed. These phases remain stable. LiH and MgB_2 are observed as the main reaction products.

From the beginning, during the entire in situ SR-XPD measurement, no TiF_4 or any Ti-containing phases could be detected (Figures 3 and S2). This suggests that Ti or any Ti-containing compounds might be present in the sample in amorphous or nanocrystalline state. Therefore, X-ray absorption spectroscopy (XAS) measurements were carried out to determine the chemical state of Ti in the doped composite system. The great advantage of XAS technique is that it is independent of the crystallinity or the amorphous state of any given sample.

XAS Measurements: Chemical State and Local Environment of Titanium. Near-edge structure (XANES) of the XAS spectra of Ti in $2LiBH_4 + MgH_2 + 0.1TiF_4$ system at different hydrogenation state was extracted to determine the respective valance states of Ti (Figure S3, Supporting Information). TiF_4 and TiB_2 samples were measured as reference compounds. A comparison among TiF_4 spectrum, TiB_2 spectrum, and the spectra of $2LiBH_4 + MgH_2 + 0.1TiF_4$ samples at different hydrogenation states reveals significant changes in the oxidation state of Ti in the hydride matrix. The oxidation state of Ti in the milled sample shows high dissimilarity to the TiF_4 reference sample. This suggests a change in the oxidation state of Ti already during the ball milling process. Thereafter, this oxidation state remains stable

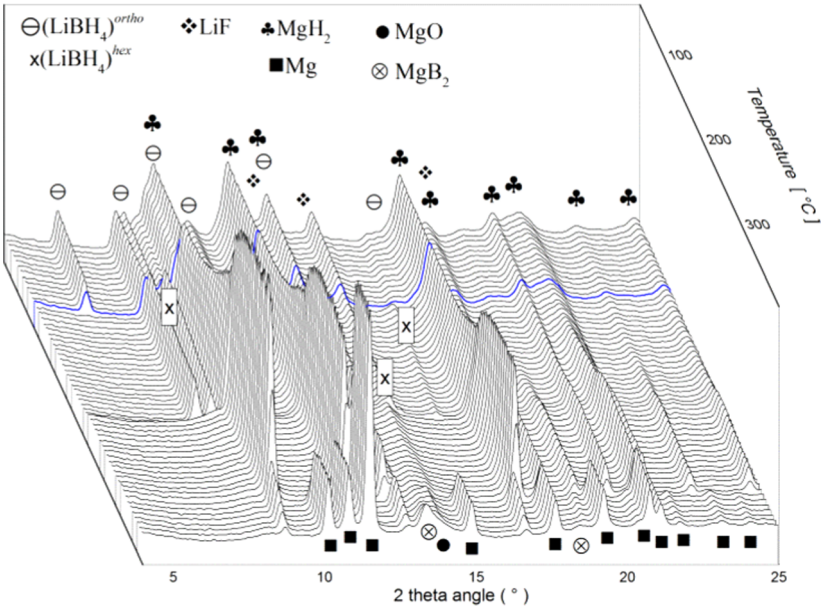

Figure 3. In situ SR-XPD for the first dehydrogenation reaction of $2LiBH_4 + MgH_2 + 0.1TiF_4$ under 4 bar H_2 backpressure. The temperature was increased with a ramp of 3 °C/min from RT to a maximum temperature of 400 °C.

DOI: 10.1021/acs.jpcc.8b02258
J. Phys. Chem. C XXXX, XXX, XXX−XXX

upon further de/rehydrogenation processes. On the other hand, the XANES spectra of the doped sample at different hydrogenation states have high similarity to the reference spectrum of TiB_2.

To further investigate the local environment of Ti atoms in the hydride matrix with respect to hydrogenation cycles, the extended X-ray absorption fine structure (EXAFS) ($\chi(k)$) region of the respective spectra was extracted and Fourier transformed. Figure 4 displays the unweighted $\chi(k)$ (in the k-range from 0 to 6 Å) for $2LiBH_4 + MgH_2 + 0.1TiF_4$ samples together with the reference spectra of TiF_4 and TiB_2.

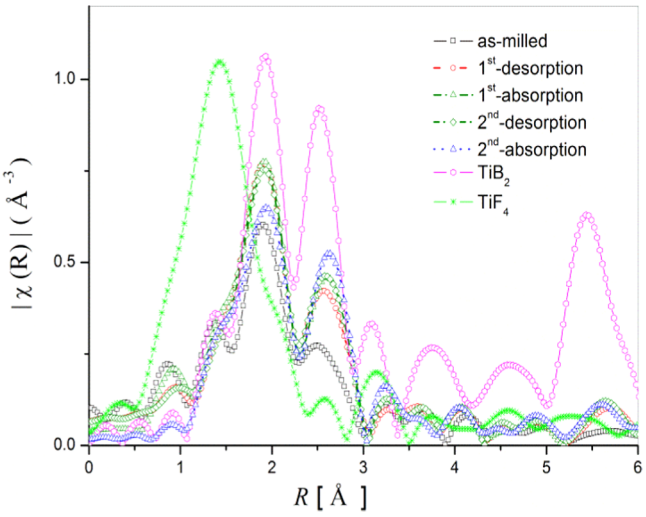

Figure 4. Fourier transformation of the EXAFS function in the k-range of [0–6] $Å^{-1}$ of Ti-containing hydride matrix at different hydrogenation cycles together with the reference spectra.

The local environment of Ti in $2LiBH_4 + MgH_2$ composite system shows considerable changes after the ball milling process. The shift in the position of the main amplitude of Ti spectra of the samples relatively to TiF_4 spectrum hints at the removal of fluorine atoms and the presence of other species as the nearest neighborhood (NN). Moreover, substantial drop in the amplitudes behind the principle amplitude around the central Ti atom, in comparison to the reference sample, is observed, indicating a high degree of disorder/dispersion of Ti-containing particles (nanosized structures). After first dehydrogenation, the principle EXAFS amplitudes are increased and remain relatively stable upon further de/rehydrogenation processes. This hints to a higher degree of ordering and/or slight growing of Ti-containing structures relative to the ball milled samples. Furthermore, a comparison between the FT-EXAF-spectra and the reference spectrum of TiB_2 shows a good correspondence over the entire R-range, indicating the presence of B as NN of the central Ti atom.

To verify the formation of TiB_2 in the doped samples at different hydrogenation states, ab initio calculations were carried out using the FEFF6 program.[61] The results of these calculation together with the EXAFS spectra of the samples are presented in Figure 5. In the calculation, the magnitudes of scattering amplitudes were not corrected for electron relaxation processes because the existence of TiB_2 phase is the center of interest. FEFF calculations were performed assuming the crystalline state of TiF_4 (space group *Pnma*; Cryst. Sys. Orthorhombic, ICSD #78737) and the crystalline state of TiB_2 (space group *P6/mmm*; Cryst. Sys. Hexagonal, ICSD #30330).

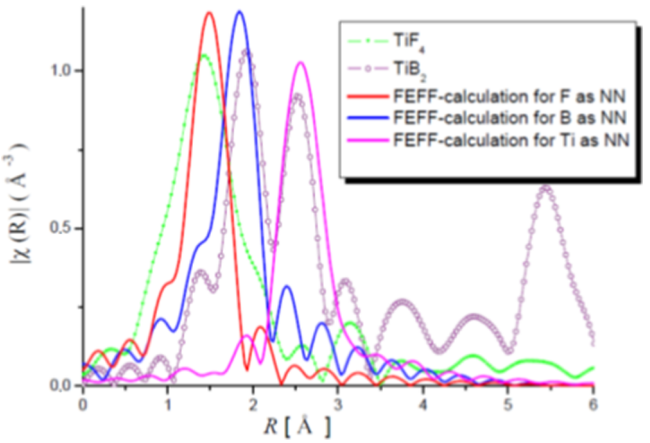

Figure 5. R-Distribution function of Ti-containing compounds in the hydride matrix after the first hydrogenation cycle and the corresponding FEFF fits.

The calculations allocate the first peak of TiF_4 to fluorine backscattering amplitude, and the first and second peaks of TiB_2 reference are addressed to boron and Ti backscattering amplitudes, respectively. This clarifies the transformation from TiF_4 to TiB_2 during the milling process of $2LiBH_4 + MgH_2 + 0.1TiF_4$ material, which remains stable upon further de/rehydrogenation cycles. To determine the size distribution of TiB_2 particles in the hydride matrix, ASAXS measurements were conducted.

ASAXS Measurements: Size Distribution of TiB_2 Particles. Anomalous Small-Angle X-ray Scattering (ASAXS) measurements in the vicinity of titanium K-absorption edge were carried out. The scattering intensities were collected at four precalculated X-ray energies (see Table 1, Experimental Section) to separate the resonant scattering curves of Ti-containing structures in the hydride matrix at different hydrogenation stages. In Figure S4 (Supporting Information), the ASAXS curves of as-milled $2LiBH_4 + MgH_2 + 0.1TiF_4$ material are displayed. The anomalous scattering effect is clearly visible as the energy of incident beam increases (Figure S4—inset plot, Supporting Information). At higher q values, a stronger energy dependency of scattering intensities is observed. This is due to fluorescence and resonant Raman scattering. This incoherent scattering causes a constant background at the very high q-values of the scattering curves, which was removed before analyzing the data. This was done by subtracting a constant value from all the ASAXS curves, so that the scattering curves at very high q values follow the Porod law afterward.[65] Exemplarily, for all other curves, the resonant scattering curve of the as-milled sample together with its corresponding total scattering and mixed resonant scattering curve are shown in Figure S5 (Supporting Information). The resonant scattering curves were fitted by using the program Gnom.[66,67] Distance distribution functions of TiB_2 particles were calculated for all the samples, assuming spherical particles. The results of these calculations are presented in Figure 6. The maxima of the curves indicate the most frequent sizes of titanium-containing structures in the samples, whereas the tail of the distance distribution function denotes the largest titanium-containing structures.

In the as-milled $2LiBH_4 + MgH_2 + 0.1TiF_4$ sample, the most frequent TiB_2 particle sizes are about 7 nm, which grow up to ~13 nm with the first dehydrogenation process. After the first

DOI: 10.1021/acs.jpcc.8b02258
J. Phys. Chem. C XXXX, XXX, XXX−XXX

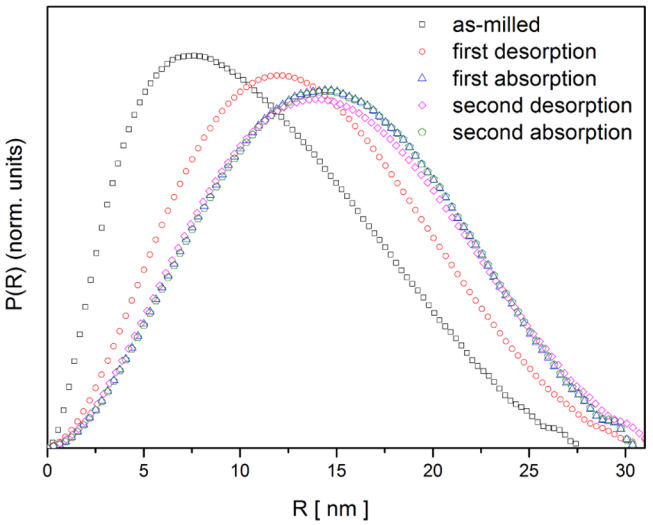

Figure 6. Distance–distribution curves of $2LiBH_4 + MgH_2 + 0.1TiF_4$ material at different hydrogenation states.

absorption, a further growth of Ti structures from 13 nm to approximately 16 nm is observed, which remains stable upon further re/dehydrogenation cycling. The largest structures in the as-milled doped sample are about 27 nm, which grow up to ~30 nm with the desorption process and remain relatively stable upon further cycling.

TEM Observations: Morphological, Nanoscopic, Structural, and Phase Characterization. An electron diffraction pattern was taken to find the most feasible phases (Figure S6, Supporting Information). The rings are correlated with the $d_{(hkl)}$ values taking into account the intensity of the rings. As seen, MgB_2 is detected, which is part of the matrix material. MgO is also present, and its presence can be attributed to the short exposure of the sample to air during TEM preparation procedure. LiF phase is detected as well, as it was shown by in situ SR-XPD measurements. Moreover, TiB_2 is clearly detected by the presence of a ring, which can be only ascribed to TiB_2 phase. In Figure 7, dark field (DF) TEM images and particles size distributions of $2LiBH_4 + MgH_2$ (Figure 7A) and $2LiBH_4 + MgH_2 + 0.1TiF_4$ (Figure 7B) samples after dehydrogenation

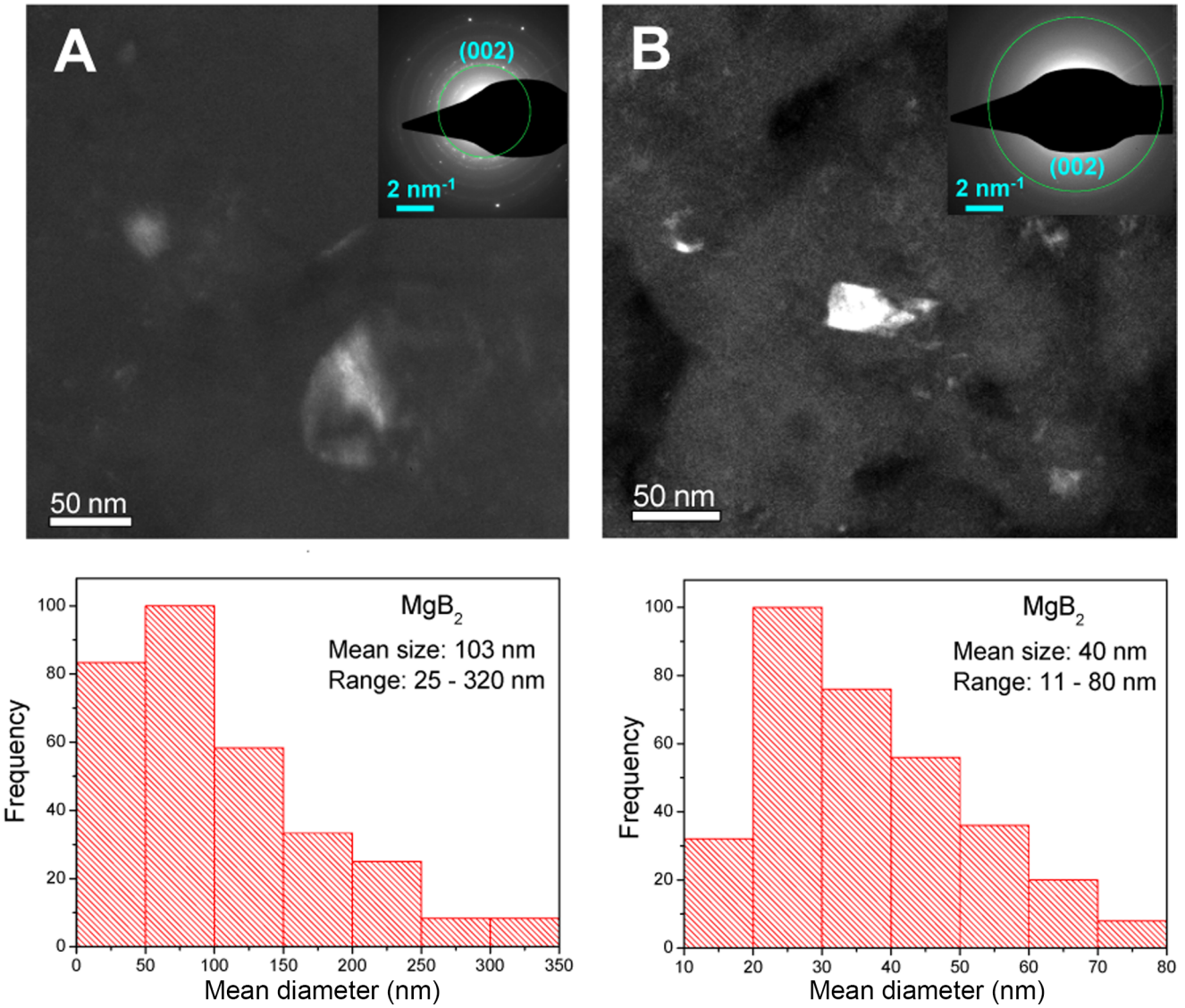

Figure 7. TEM in dark field (DF) modus (top) and MgB_2 particle size distribution (bottom) in $2LiBH_4 + MgH_2$ (left) and $2LiBH_4 + MgH_2 + 0.1TiF_4$ (right).

DOI: 10.1021/acs.jpcc.8b02258
J. Phys. Chem. C XXXX, XXX, XXX–XXX

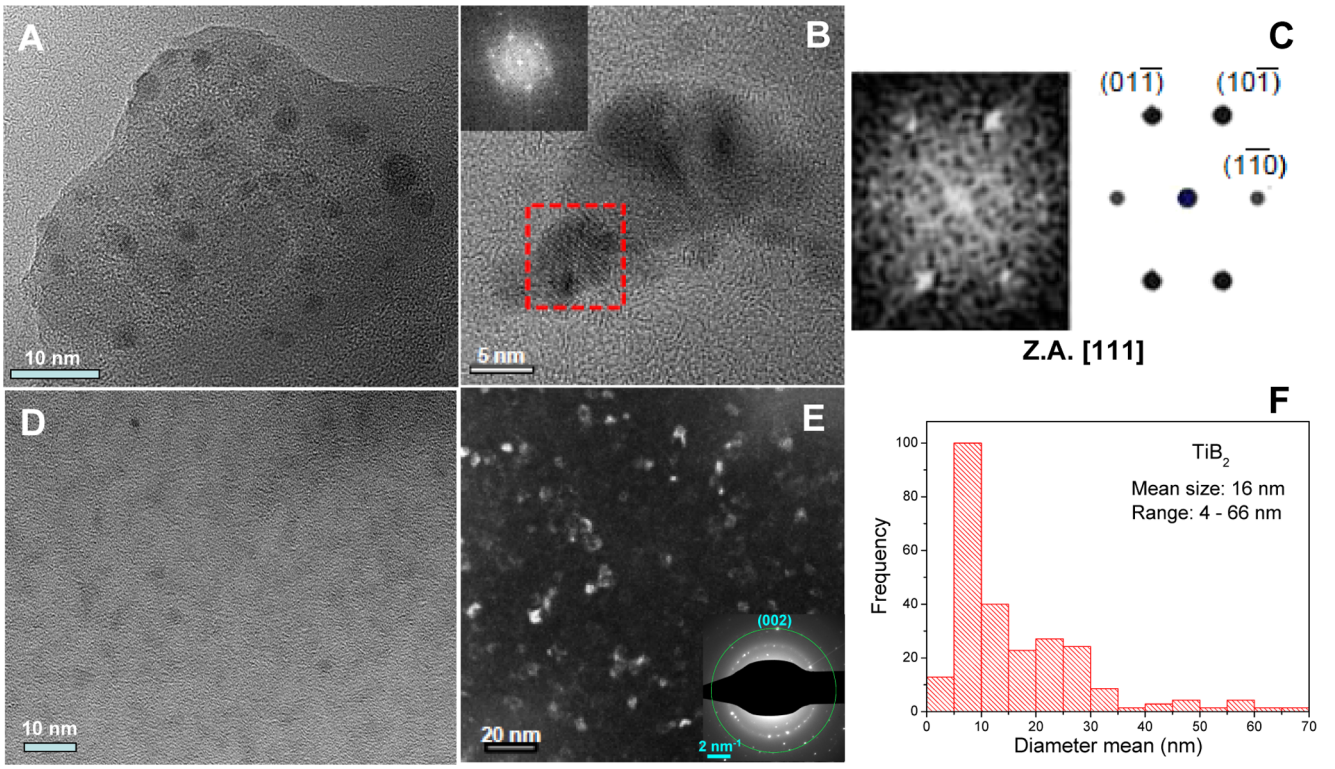

Figure 8. $2LiBH_4 + MgH_2 + 0.1TiF_4$ after the first dehydrogenation: (A, B) HR-TEM images. (C) FT and structure simulation. (D) Bright field. (E) Dark field in the shown bright field region and inset plot of the diffraction used for the DF. (F) Particle size distribution of TiB_2.

are shown. It can be observed that the MgB_2 particles in $2LiBH_4 + MgH_2$ sample are in average about 100 nm in size, whereas the average MgB_2 particles in the doped sample are around 40 nm. Figure 8 shows the HR-TEM images in bright field (Figure 8A,B,D) and in dark field (Figure 8E) for $2LiBH_4 + MgH_2 + 0.1TiF_4$ material after the first dehydrogenation. Additionally, the Fourier transform of a particle (Figure 8B) and the corresponding simulation along with the resulting particle size distribution are exhibited (Figure 8C,F). From the HR-TEM images, it is possible to verify the presence of small particles of TiB_2 in $2LiBH_4 + MgH_2 + 0.1TiF_4$ after the first dehydrogenation. The FT analysis (Figure 8C) is in agreement with the electron pattern simulation, thus confirming that TiB_2 particles are formed. This result is in accordance with the XAS analysis. From the DF image, size measurements have been carried out on numerous particles, leading to quite a reliable size distribution. The TiB_2 structures show reduced sizes compared to those from MgB_2 particles. As it is observed, the average particle size of TiB_2 is about 16 nm, with a range between 4 and 66 nm. These TiB_2 nanosizes are in good agreement with the ASAXS results (Figure 6).

DISCUSSION

The addition of TiF_4 significantly improves the dehydrogenation/hydrogenation kinetics of $2LiBH_4 + MgH_2$ composite system (Figures 1 and S1, Supporting Information). During the first nonisothermal dehydrogenation, the presence of TiF_4 precludes the long plateau period. This plateau phase is observed in pristine Li-RHC system and proceeds with almost no hydrogen release. It was reported before that this plateau phase might account for a slow incubation period required for the nucleation of MgB_2 seeds.[43] However, based on the experimental evidence, it was recently found that the plateau phase during the first dehydrogenation of the Li-RHC system is due to the slow formation of small amount of $Li_2B_{12}H_{12}$ from $LiBH_4$ according to the reaction: $2LiBH_4 \rightarrow (1/6)Li_2B_{12}H_{12} + (5/3)LiH + (13/6)H_2$.[68−70] The formation of $Li_2B_{12}H_{12}$ partially blocks the interaction between $LiBH_4$ and Mg, and the formation of MgB_2 is delayed.[71] Moreover, the formation of gaseous B_2H_6, which further interacts with LiH, can lead to the formation of $Li_2B_{12}H_{12}$. However, the presence of backpressure during dehydrogenation can kinetically avoid the formation of gaseous diborane (B_2H_6) as an intermediate.[17,72,73] To shed some light on the nature of the plateau region, TiB_2 powder was ball milled for 10 h. Subsequently, $0.1TiB_2$ (premilled powder) was added to MgH_2, which was already milled for 5 h. Thereafter, $LiBH_4$ was added to the mixture and the entire composite system ($2LiBH_4 + MgH_2 + 0.1TiB_2$) was further milled for additional 5 h.

The dehydrogenation kinetics of $2LiBH_4 + MgH_2 + 0.1TiB_2$ system was measured by means of volumetric method. The results show (Figure S7, Supporting Information) that the plateau phase is significantly reduced by the presence of as-milled TiB_2. However, the plateau region does not disappear completely. Therefore, it is possible to infer that there must be some formation of $Li_2B_{12}H_{12}$ coming from the initial $LiBH_4$ decomposition and the amorphous boron in the starting material (Figure S8, Supporting Information). Despite this fact, the presence of TiB_2 provides more centers for the nucleation of MgB_2, promoting the early formation and fast growth of this phase and thus majorly avoiding an excessive growth of the $Li_2B_{12}H_{12}$ barrier that would delay the formation of MgB_2. For the case of $2LiBH_4 + MgH_2 + 0.1TiF_4$, the nature of the in situ formed nanoparticles of TiB_2 is more effective because the plateau region is totally suppressed (Figures 1 and S7). This can be ascribed to the nanostructured TiB_2 and the better

DOI: 10.1021/acs.jpcc.8b02258
J. Phys. Chem. C XXXX, XXX, XXX−XXX

distribution of nucleation centers for MgB_2. These experimental results and analyses allow inferring that the formation of $Li_2B_{12}H_{12}$ and the nucleation of MgB_2 seeds are two competing reactions upon the decomposition of $LiBH_4$ in the Li-RHC. Upon cycling, it is noticed that the presence of the additive causes a drop in the hydrogen capacity from about 10 wt % H_2 to 8 wt % H_2 in comparison to pristine $2LiBH_4 + MgH_2$ (Figure 2). Nevertheless, the enhanced kinetic behavior and hydrogen capacity of 8 wt % remain stable.

In previous works, it was found that the interaction of $3LiBH_4/1TiF_3$ stoichiometric mixture during milling leads to the formation of volatile $Ti(BH_4)_3$.[74,75] Kang et al.[76] showed the formation of nanosized TiB_2 by the interaction between $LiBH_4$ and TiF_3. They found that a one-step milling process leads to the partial formation of TiB_2. However, a three-step method starting with a $1LiBH_4/0.04TiF_3$ stoichiometric mixture provided the full conversion to nanosized TiB_2. In this work, a one-step milling procedure provides the full conversion to nanosized TiB_2 (Figures 4, 5, and 8) from the interaction between $2LiBH_4 + MgH_2$ material and $0.1TiF_4$ additive.

To understand the interactions between $2LiBH_4 + MgH_2$ composite material and TiF_4, phase composition equilibrium calculations based on the Gibbs free energy minimization were carried out with the HSC Chemistry software.[63] The calculations under different conditions such as mechanical milling, first dehydrogenation, and first hydrogenation were performed (Table S1, Supporting Information). The equilibrium calculations predict that after milling, the formation of LiF, TiB_2, and B is thermodynamically favored according to the reaction (4): $0.4LiBH_4 + 0.1TiF_4 \rightarrow 0.4LiF + 0.1TiB_2 + 0.2B + 0.8H_{2(g)}$ ($\Delta G_{298K} = -57.2$ kJ).

In situ SR-XPD shows the presence of LiF after milling (Figure 3). Moreover, after milling, the crystallite size of MgH_2 in $2LiBH_4 + MgH_2 + 0.1TiF_4$ sample is further refined down to 8 nm in comparison with 15 nm for $2LiBH_4 + MgH_2$ (Supporting Information Figure S9, ex situ XRD). The NMR results (Figure S8, Supporting Information) evidence the presence of amorphous boron and boride compounds in the as-purchased $LiBH_4$. For the as-milled $2LiBH_4 + MgH_2 + 0.1TiF_4$, the amount of amorphous boron increases. Moreover, mass spectroscopy measurements show the presence of hydrogen in the milling chamber atmosphere (Figure S10, Supporting Information). These results are in accordance with the proposed reaction (4). Upon dehydrogenation and hydrogenation, the experimental results (Figures 3−5, and 8) and the equilibrium thermodynamic calculation show that LiF and TiB_2 remain stable under the applied conditions. This explains the reduction in the gravimetric hydrogen storage capacity of $2LiBH_4 + MgH_2 + 0.1TiF_4$ composite system in comparison to the pure Li-RHC. Furthermore, size distribution of TiB_2 structures was determined via ASAXS measurements and TEM observations (Figures 6 and 8). Both methods show roughly a size distribution of TiB_2 nanoparticles with sizes around 10−16 nm. These TiB_2 nanoparticles are most likely responsible for the heterogeneous nucleation and the growth of MgB_2 phase during the dehydrogenation of $2LiBH_4$-Mg. Calculations, carried out based on the mismatch theory,[77,78] revealed two possible crystallographic matching planes between TiB_2 and MgB_2 ($MgB_2\{1010\}//TiB_2\{1010\}$ = 1.9 and $MgB_2\{1011\}//TiB_2\{1011\}$ = 4.5). These mismatch values are lower than 6%, which is considered as the upper limit value.[79] Therefore, TiB_2 can provide two possible crystallographic nucleation planes for MgB_2. This assumption is further indirectly verified by the results obtained via TEM observation of MgB_2 particle size distributions in the matrix of pure and doped composite system (Figure 7). In the doped system, the average MgB_2 particle size is about 40 nm and the maximum observed MgB_2 particle size range is roughly 80 nm, whereas in the pure material, the corresponding average size is about 100 nm and the maximum size is around 300 nm. This observation can be explained by assuming the uniformly distributed TiB_2 nanoparticles in the hydride matrix that act as nucleation centers for MgB_2 phase during dehydrogenation. Thus, MgB_2 seeds start to nucleate and grow around these nuclei. Due to the vast numbers of these nucleation centers, which are uniformly distributed in the material with additive, the nucleation of MgB_2 starts to take place in numerous places in the interface of $LiBH_4$/Mg. This mechanism, indeed, leads to notably faster reaction kinetics and significantly smaller MgB_2 structures, in comparison to the corresponding pure Li-RHC system.

CONCLUSIONS

One-step in situ synthesis of nanosized TiB_2 from the interaction between $LiBH_4$ and TiF_4 is observed. During the ball milling procedure, nanosized TiB_2 is formed and remains stable upon dehydrogenation/hydrogenation cycling.

The presence of nanosized TiB_2 notably improves the kinetic behavior of $2LiBH_4 + MgH_2$ system by reducing the dehydrogenation and hydrogenation times from 10−20 h to less than 3 h and from 8 h to about 1 h, respectively. Moreover, the Li-RHC system doped with $0.1TiF_4$ shows a reversible hydrogen capacity of 8 wt %. The observed kinetic improvement of the doped system accounts for its refined microstructure, homogeneous distribution of nanosized TiB_2, and the feasibility of TiB_2 to act as the nucleation interface for MgB_2.

ASSOCIATED CONTENT

Supporting Information

The Supporting Information is available free of charge on the ACS Publications website at DOI: 10.1021/acs.jpcc.8b02258.

Additional results for $2LiBH_4 + MgH_2 + 0.1TiF_4$; coupled volumetric and calorimetric HP-DSC, in situ SR-XRD for the dehydrogenation reaction at isothermal condition, XANES structure at different hydrogenation state, ASAXS scattering curves, TEM after dehydrogenation with the corresponding table of the reflections; MS measurements; volumetric measurements; nonisothermal dehydrogenation of $2LiBH_4 + MgH_2$, $2LiBH_4 + MgH_2 + 0.1TiF_4$, and $2LiBH_4 + [(MgH_2 + 0.1TiB_2)$ premilled] samples; thermodynamic equilibrium calculations; ex situ XRD and NMR of the as-purchased $LiBH_4$ and the as-milled $2LiBH_4 + MgH_2 + 0.1TiF_4$ (PDF)

AUTHOR INFORMATION

Corresponding Author

*E-mail: julian.puszkiel@hzg.de. Tel.: +4917621631783.

ORCID

Fahim Karimi: 0000-0001-6220-1463

Antonio Santoru: 0000-0003-2619-7481

Pau Nolis: 0000-0003-2360-1709

DOI: 10.1021/acs.jpcc.8b02258
J. Phys. Chem. C XXXX, XXX, XXX−XXX

Author Contributions

The authors of this manuscript substantially contributed to this work. The final version of this manuscript was reviewed by all the authors. This manuscript is submitted by agreement of all the authors.

Notes

The authors declare no competing financial interest.

■ ACKNOWLEDGMENTS

The authors thank CONICET (Consejo Nacional de Invetigaciones Científicas y Técnicas), ANPCyT (Agencia Nacional de Promoción Científica y Tecnológica) PICT 2015−1865, CNEA (Comisión Nacional de Energía Atómica), for financial support to carry out this work. We would also like to thank the Metals Physics Division at HZG for providing the TEM devices. We thank HZB for the allocation of synchrotron radiation beamtime. The research leading to these results has received funding from the European Marie Curie Actions under ECOSTORE grant agreement no. 607040.

■ ABBREVIATIONS

RHC, reactive hydride composite; SR-XPD, synchrotron radiation X-ray powder diffraction; XAS, X-ray absorption spectroscopy; ASAXS, anomalous small-angle X-ray scattering; MS, mass spectroscopy

■ REFERENCES

(1) Züttel, A.; Borgschule, A.; Schlapbach, A. *Hydrogen as a Future Energy Carrier*; John Wiley & Sons: New York, 2008.

(2) Schlapbach, L.; Züttel, A. Hydrogen-Storage Materials for Mobile Applications. *Nature* **2001**, *414*, 353.

(3) Schüth, F.; Bogdanovic, B.; Felderhoff, M. Light Metal Hydrides and Complex Hydrides for Hydrogen Storage. *Chem. Commun.* **2004**, 2249−2258.

(4) Züttel, A.; Wenger, P.; Rentsch, S.; Sudan, P.; Mauron, P.; Emmenegger, C. $LiBH_4$ a New Hydrogen Storage Material. *J. Power Sources* **2003**, *118*, 1−7.

(5) Züttel, A.; Rentsch, S.; Fischer, P.; Wenger, P.; Sudan, P.; Mauron, P.; Emmenegger, C. Hydrogen Storage Properties of $LiBH_4$. *J. Alloys Compd.* **2003**, *356-357*, 515−520.

(6) Ohba, N.; Miwa, K.; Aoki, M.; Noritake, T.; Towata, S.-i.; Nakamori, Y.; Orimo, S.-i.; Züttel, A. First-Principles Study on the Stability of Intermediate Compounds of $LiBH_4$. *Phys. Rev. B* **2006**, *74*, No. 075110.

(7) Au, M.; Jurgensen, A.; Zeigler, K. Modified Lithium Borohydrides for Reversible Hydrogen Storage (2). *J. Phys. Chem. B* **2006**, *110*, 26482−26487.

(8) Kang, X.-D.; Wang, P.; Ma, L.-P.; Cheng, H.-M. Reversible Hydrogen Storage in $LiBH_4$ Destabilized by Milling with Al. *Appl. Phys. A* **2007**, *89*, 963.

(9) Hwang, S.-J.; Bowman, R. C.; Reiter, J. W.; Rijssenbeek; Soloveichik, G. L.; Zhao, J.-C.; Kabbour, H.; Ahn, C. C. Nmr Confirmation for Formation of $[B_{12}H_{12}]^{2-}$ Complexes During Hydrogen Desorption from Metal Borohydrides. *J. Phys. Chem. C* **2008**, *112*, 3164−3169.

(10) Zhang, Y.; Zhang, W.-S.; Fan, M.-Q.; Liu, S.-S.; Chu, H.-L.; Zhang, Y.-H.; Gao, X.-Y.; Sun, L.-X. Enhanced Hydrogen Storage Performance of $LiBH_4$−SiO_2−TiF_3 Composite. *J. Phys. Chem. C* **2008**, *112*, 4005−4010.

(11) Mosegaard, L.; Møller, B.; Jørgensen, J.-E.; Filinchuk, Y.; Cerenius, Y.; Hanson, J. C.; Dimasi, E.; Besenbacher, F.; Jensen, T. R. Reactivity of $LiBH_4$: In Situ Synchrotron Radiation Powder X-Ray Diffraction Study. *J. Phys. Chem. C* **2008**, *112*, 1299−1303.

(12) Au, M.; Jurgensen, A. R.; Spencer, W. A.; Anton, D. L.; Pinkerton, F. E.; Hwang, S.-J.; Kim, C.; Bowman, R. C. Stability and Reversibility of Lithium Borohydrides Doped by Metal Halides and Hydrides. *J. Phys. Chem. C* **2008**, *112*, 18661−18671.

(13) Xu, J.; Yu, X.; Zou, Z.; Li, Z.; Wu, Z.; Akins, D. L.; Yang, H. Enhanced Dehydrogenation of $LiBH_4$ Catalyzed by Carbon-Supported Pt Nanoparticles. *Chem. Commun.* **2008**, 5740−5742.

(14) Fang, Z.-Z.; Kang, X.-D.; Wang, P.; Cheng, H.-M. Improved Reversible Dehydrogenation of Lithium Borohydride by Milling with as-Prepared Single-Walled Carbon Nanotubes. *J. Phys. Chem. C* **2008**, *112*, 17023−17029.

(15) Xia, G. L.; Guo, Y. H.; Wu, Z.; Yu, X. B. Enhanced Hydrogen Storage Performance of $LiBH_4$−Ni Composite. *J. Alloys Compd.* **2009**, *479*, 545−548.

(16) Caputo, R.; Züttel, A. First-Principles Study of the Paths of the Decomposition Reaction of $LiBH_4$. *Mol. Phys.* **2010**, *108*, 1263−1276.

(17) Friedrichs, O.; Remhof, A.; Hwang, S. J.; Züttel, A. Role of $Li_2B_{12}H_{12}$ for the Formation and Decomposition of $LiBH_4$. *Chem. Mater.* **2010**, *22*, 3265−3268.

(18) Ngene, P.; van Zwienen, M.; de Jongh, P. E. Reversibility of the Hydrogen Desorption from $LiBH_4$: A Synergetic Effect of Nanoconfinement and Ni Addition. *Chem. Commun.* **2010**, *46*, 8201−8203.

(19) Rude, L. H.; Groppo, E.; Arnbjerg, L. M.; Ravnsbæk, D. B.; Malmkjær, R. A.; Filinchuk, Y.; Baricco, M.; Besenbacher, F.; Jensen, T. R. Iodide Substitution in Lithium Borohydride, $LiBH_4$−LiI. *J. Alloys Compd.* **2011**, *509*, 8299−8305.

(20) Zavorotynska, O.; Corno, M.; Pinatel, E.; Rude, L. H.; Ugliengo, P.; Jensen, T. R.; Baricco, M. Theoretical and Experimental Study of $LiBH_4$-LiCl Solid Solution. *Crystals* **2012**, *2*, 144.

(21) Shao, J.; Xiao, X.; Fan, X.; Zhang, L.; Li, S.; Ge, H.; Wang, Q.; Chen, L. Low-Temperature Reversible Hydrogen Storage Properties of $LiBH_4$: A Synergetic Effect of Nanoconfinement and Nanocatalysis. *J. Phys. Chem. C* **2014**, *118*, 11252−11260.

(22) Orimo, S.-I.; Nakamori, Y.; Ohba, N.; Miwa, K.; Aoki, M.; Towata, S.-i.; Züttel, A. Experimental Studies on Intermediate Compound of $LiBH_4$. *Appl. Phys. Lett.* **2006**, *89*, No. 021920.

(23) Orimo, S.; Nakamori, Y.; Eliseo, J. R.; Züttel, A.; Jensen, C. M. Complex Hydrides for Hydrogen Storage. *Chem. Rev.* **2007**, *107*, 4111−4132.

(24) Mauron, P.; Buchter, F.; Friedrichs, O.; Remhof, A.; Bielmann, M.; Zwicky, C. N.; Züttel, A. Stability and Reversibility of Libh4. *J. Phys. Chem. B* **2008**, *112*, 906−910.

(25) Fedneva, E. M.; Alpatova, V. I.; Mikheeva, V. I. Transl. of Zh. Neorg. Khim. *Russ. J. Inorg. Chem.* **1964**, *9*, 826−827.

(26) Barkhordarian, G.; Klassen, T.; Bormann, R. German Patent DE1022004/061286, 2004.

(27) Vajo, J. J.; Skeith, S. L.; Mertens, F. Reversible Storage of Hydrogen in Destabilized $LiBH_4$. *J. Phys. Chem. B* **2005**, *109*, 3719−3722.

(28) Bösenberg, U.; et al. Hydrogen Sorption Properties of Mgh2−Libh4 Composites. *Acta Mater.* **2007**, *55*, 3951−3958.

(29) Pistidda, C.; et al. Effect of the Partial Replacement of Cah2 with Caf2 in the Mixed System CaH_2 + MgB_2. *J. Phys. Chem. C* **2014**, *118*, 28409−28417.

(30) Bergemann, N.; Pistidda, C.; Milanese, C.; Emmler, T.; Karimi, F.; Chaudhary, A. L.; Chierotti, M. R.; Klassen, T.; Dornheim, M. $Ca(BH_4)_2$-Mg_2NiH_4: On the Pathway to a $Ca(BH_4)_2$ System with a Reversible Hydrogen Cycle. *Chem. Commun.* **2016**, *52*, 4836−4839.

(31) Sale, M.; Pistidda, C.; Taras, A.; Napolitano, E.; Milanese, C.; Karimi, F.; Dornheim, M.; Garroni, S.; Enzo, S.; Mulas, G. In Situ Synchrotron Radiation Powder X-Ray Diffraction Study of the $2LiNH_2$ + LiH + KBH_4 System. *J. Alloys Compd.* **2013**, *580*, S278−S281.

(32) Gosalawit−Utke, R.; et al. $LiBH_4$−MgH_2 in a Resorcinol−Furfural Carbon Aerogel Scaffold for Reversible Hydrogen Storage. *J. Phys. Chem. C* **2012**, *116*, 1526−1534.

(33) Cao, H.; et al. Kinetic Alteration of the $6Mg(NH_2)_2$-9LiH-$LiBH_4$ System by Co-Adding YCl_3 and Li_3N. *Phys. Chem. Chem. Phys.* **2017**, *19*, 32105−32115.

(34) Carrillo-Bucio, J. L.; Saldan, I.; Pistidda, C.; Karimi, F.; Suárez-Alcántara, K.; Dornheim, M.; Klassen, T. Hydrogenation Study of

DOI: 10.1021/acs.jpcc.8b02258
J. Phys. Chem. C XXXX, XXX, XXX−XXX

NaF/NaH/MgB_2 Reactive Hydride Composites. *J. Phys. Chem. C* **2017**, *121*, 4093−4102.
(35) Santoru, A.; et al. KNH_2-KH: A Metal Amide-Hydride Solid Solution. *Chem. Commun.* **2016**, *52*, 11760−11763.
(36) Karimi, F.; et al. Structural and Kinetic Investigation of the Hydride Composite $Ca(BH_4)_2$ + MgH_2 System Doped with Nbf5 for Solid-State Hydrogen Storage. *Phys. Chem. Chem. Phys.* **2015**, *17*, 27328−27342.
(37) Karimi, F.; Pranzas, P. K.; Hoell, A.; Vainio, U.; Welter, E.; Raghuwanshi, V. S.; Pistidda, C.; Dornheim, M.; Klassen, T.; Schreyer, A. Structural Analysis of Calcium Reactive Hydride Composite for Solid State Hydrogen Storage. *J. Appl. Crystallogr.* **2014**, *47*, 67−75.
(38) Gosalawit-Utke, R.; Milanese, C.; Nielsen, T. K.; Karimi, F.; Saldan, I.; Pranzas, K.; Jensen, T. R.; Marini, A.; Klassen, T.; Dornheim, M. Nanoconfined 2$LiBH_4$−MgH_2 for Reversible Hydrogen Storages: Reaction Mechanisms, Kinetics and Thermodynamics. *Int. J. Hydrogen Energy* **2013**, *38*, 1932−1942.
(39) Puszkiel, J.; et al. Sorption Behavior of the MgH_2−Mg_2FeH_6 Hydride Storage System Synthesized by Mechanical Milling Followed by Sintering. *Int. J. Hydrogen Energy* **2013**, *38*, 14618−14630.
(40) Pinkerton, F. E.; Meyer, M. S.; Meisner, G. P.; Balogh, M. P.; Vajo, J. J. Phase Boundaries and Reversibility of $LiBH_4$/MgH_2 Hydrogen Storage Material. *J. Phys. Chem. C* **2007**, *111*, 12881−12885.
(41) Bösenberg, U.; Ravnsbæk, D. B.; Hagemann, H.; D'Anna, V.; Minella, C. B.; Pistidda, C.; van Beek, W.; Jensen, T. R.; Bormann, R.; Dornheim, M. Pressure and Temperature Influence on the Desorption Pathway of the $LiBH_4$−MgH_2 Composite System. *J. Phys. Chem. C* **2010**, *114*, 15212−15217.
(42) Puszkiel, J.; et al. Hydrogen Storage in Mg− $LiBH_4$ Composites Catalyzed by FeF_3. *J. Power Sources* **2014**, *267*, 799−811.
(43) Bösenberg, U.; et al. Role of Additives in $LiBH_4$−MgH_2 Reactive Hydride Composites for Sorption Kinetics. *Acta Mater.* **2010**, *58*, 3381−3389.
(44) Sun, T.; Wang, H.; Zhang, Q.; Sun, D.; Yao, X.; Zhu, M. Synergetic Effects of Hydrogenated Mg_3La and $TiCl_3$ on the Dehydrogenation of $LiBH_4$. *J. Mater. Chem.* **2011**, *21*, 9179−9184.
(45) Mao, J.; Guo, Z.; Yu, X.; Liu, H. Improved Reversible Dehydrogenation of 2 $LiBH_4$ + MgH_2 System by Introducing Ni Nanoparticles. *J. Mater. Res.* **2011**, *26*, 1143−1150.
(46) Deprez, E.; Muñoz-Márquez, M. A.; Haro, M. C. J. d; Palomares, F. J.; Soria, F.; Dornheim, M.; Bormann, R.; Fernández, A. Combined X-Ray Photoelectron Spectroscopy and Scanning Electron Microscopy Studies of the $LiBH_4$−MgH_2 Reactive Hydride Composite with and without a Ti-Based Additive. *J. Appl. Phys.* **2011**, *109*, No. 014913.
(47) Deprez, E.; Justo, A.; Rojas, T. C.; López-Cartés, C.; Bonatto Minella, C.; Bösenberg, U.; Dornheim, M.; Bormann, R.; Fernández, A. Microstructural Study of the $LiBH_4$−MgH_2 Reactive Hydride Composite with and without Ti-Isopropoxide Additive. *Acta Mater.* **2010**, *58*, 5683−5694.
(48) Kou, H.; Xiao, X.; Li, J.; Li, S.; Ge, H.; Wang, Q.; Chen, L. Effects of Fluoride Additives on Dehydrogenation Behaviors of 2 $LiBH_4$ + MgH_2 System. *Int. J. Hydrogen Energy* **2012**, *37*, 1021−1026.
(49) Xiao, X.; Shao, J.; Chen, L.; Kou, H.; Fan, X.; Deng, S.; Zhang, L.; Li, S.; Ge, H.; Wang, Q. Effects of NbF_5 Addition on the De/Rehydrogenation Properties of 2$LiBH_4$/MgH_2 Hydrogen Storage System. *Int. J. Hydrogen Energy* **2012**, *37*, 13147−13154.
(50) Pranzas, P. K.; et al. Characterization of Hydrogen Storage Materials and Systems with Photons and Neutrons. *Adv. Eng. Mater.* **2011**, *13*, 730−736.
(51) Fan, X.; Xiao, X.; Chen, L.; Wang, X.; Li, S.; Ge, H.; Wang, Q. High Catalytic Efficiency of Amorphous Tib2 and NbB_2 Nanoparticles for Hydrogen Storage Using the 2$LiBH_4$−MgH_2 System. *J. Mater. Chem. A* **2013**, *1*, 11368−11375.
(52) Deprez, E.; Muñoz-Márquez, M. A.; Roldán, M. A.; Prestipino, C.; Palomares, F. J.; Minella, C. B.; Bösenberg, U.; Dornheim, M.; Bormann, R.; Fernández, A. Oxidation State and Local Structure of Ti-Based Additives in the Reactive Hydride Composite 2$LiBH_4$ + MgH_2. *J. Phys. Chem. C* **2010**, *114*, 3309−3317.
(53) Hammersley, A. P. *Fit2d: An Introduction and Overview*; ESRF: France, 1997.
(54) Bieder, H.; Hoell, A.; Mokrani, L.; Zizak, I. DE102006029449, 2007.
(55) Hoell, A.; Tatchev, D.; Haas, S.; Haug, J.; Boesecke, P. On the Determination of Partial Structure Functions in Small-Angle Scattering Exemplified by Al89ni6la5 Alloy. *J. Appl. Crystallogr.* **2009**, *42*, 323−325.
(56) Cromer, D. T.; Liberman, D. Relativistic Calculation of Anomalous Scattering Factors for X Rays. *J. Chem. Phys.* **1970**, *53*, 1891−1898.
(57) Vainio, U. *Neutrons and Synchrotron Radiation in Engineering Materials Science: From Fundamentals to Applications*, 2nd ed.; John Wiley & Sons, 2017; Vol. *217*−*225*.
(58) Goerigk, G.; Huber, K.; Schweins, R. Probing the Extent of the Sr^{2+} Ion Condensation to Anionic Polyacrylate Coils: A Quantitative Anomalous Small-Angle X-Ray Scattering Study. *J. Chem. Phys.* **2007**, *127*, No. 154908.
(59) Ravel, B.; Newville, M. Athena, Artemis, Hephaestus: Data Analysis for X-Ray Absorption Spectroscopy Using Ifeffit. *J. Synchrotron Radiat.* **2005**, *12*, 537−541.
(60) i-TEM (License N° A2382500).
(61) Micrograph Digital (License N° 90294175).
(62) JEMs (License N° Ieb59ybdflumh).
(63) Outokumpu HSC Chemistry for Windows, v., Outotec.
(64) Nakagawa, T.; Ichikawa, T.; Hanada, N.; Kojima, Y.; Fujii, H. Thermal Analysis on the Li−Mg−B−H Systems. *J. Alloys Compd.* **2007**, *446*−*447*, 306−309.
(65) Porod, G. *Die Röntgenkleinwinkelstreuung Von Dichtgepackten Kolloiden Systemen*; Springer-Verlag: Berlin, 1951; Vol. *124*.
(66) Svergun, D. Determination of the Regularization Parameter in Indirect-Transform Methods Using Perceptual Criteria. *J. Appl. Crystallogr.* **1992**, *25*, 495−503.
(67) Semenyuk, A. V.; Svergun, D. I. Gnom - a Program Package for Small-Angle Scattering Data Processing. *J. Appl. Crystallogr.* **1991**, *24*, 537−540.
(68) Yan, Y.; Li, H.-W.; Maekawa, H.; Miwa, K.; Towata, S.-i.; Orimo, S.-i. Formation of Intermediate Compound $Li_2B_{12}H_{12}$ During the Dehydrogenation Process of the $LiBH_4$−MgH_2 System. *J. Phys. Chem. C* **2011**, *115*, 19419−19423.
(69) Kim, K.-B.; Shim, J.-H.; Park, S.-H.; Choi, I.-S.; Oh, K. H.; Cho, Y. W. Dehydrogenation Reaction Pathway of the $LiBH_4$−MgH_2 Composite under Various Pressure Conditions. *J. Phys. Chem. C* **2015**, *119*, 9714−9720.
(70) Puszkiel, J. A.; Castro Riglos, M. V.; Karimi, F.; Santoru, A.; Pistidda, C.; Klassen, T.; Bellosta von Colbe, J. M.; Dornheim, M. Changing the Dehydrogenation Pathway of $LiBH_4$−MgH_2 via Nanosized Lithiated TiO_2. *Phys. Chem. Chem. Phys.* **2017**, *19*, 7455−7460.
(71) White, J. L.; Newhouse, R. J.; Zhang, J. Z.; Udovic, T. J.; Stavila, V. Understanding and Mitigating the Effects of Stable Dodecahydro-Closo-Dodecaborate Intermediates on Hydrogen-Storage Reactions. *J. Phys. Chem. C* **2016**, *120*, 25725−25731.
(72) Kim, K.-B.; Shim, J.-H.; Cho, Y. W.; Oh, K. H. Pressure-Enhanced Dehydrogenation Reaction of the $LiBH_4$-YH_3 Composite. *Chem. Commun.* **2011**, *47*, 9831−9833.
(73) Kostka, J.; Lohstroh, W.; Fichtner, M.; Hahn, H. Diborane Release from $LiBH_4$/Silica-Gel Mixtures and the Effect of Additives. *J. Phys. Chem. C* **2007**, *111*, 14026−14029.
(74) Fang, Z. Z.; Ma, L. P.; Kang, X. D.; Wang, P. J.; Wang, P.; Cheng, H. M. In Situ Formation and Rapid Decomposition of $Ti(BH_4)_3$ by Mechanical Milling $LiBH_4$ with TiF_3. *Appl. Phys. Lett.* **2009**, *94*, No. 044104.
(75) Callini, E.; Szilagyi, P. A.; Paskevicius, M.; Stadie, N. P.; Rehault, J.; Buckley, C. E.; Borgschulte, A.; Zuttel, A. Stabilization of Volatile $Ti(BH_4)_3$ by Nano-Confinement in a Metal-Organic Framework. *Chem. Sci.* **2016**, *7*, 666−672.
(76) Kang, X.; Wang, K.; Zhong, Y.; Yang, B.; Wang, P. A Novel Three-Step Method for Preparation of a Tib2-Promoted $LiBH_4$-MgH_2

DOI: 10.1021/acs.jpcc.8b02258
J. Phys. Chem. C XXXX, XXX, XXX−XXX

Composite for Reversible Hydrogen Storage. *Phys. Chem. Chem. Phys.* **2013**, *15*, 2153−2158.
(77) Zhang, M.-X.; Kelly, P. M. Edge-to-Edge Matching and Its Applications: Part I. Application to the Simple Hcp/Bcc System. *Acta Mater.* **2005**, *53*, 1073−1084.
(78) Zhang, M.-X.; Kelly, P. M. Edge-to-Edge Matching and Its Applications: Part Ii. Application to Mg−Al, Mg−Y and Mg−Mn Alloys. *Acta Mater.* **2005**, *53*, 1085−1096.
(79) Zhang, M.-X.; Kelly, P. M. Edge-to-Edge Matching Model for Predicting Orientation Relationships and Habit Planes—the Improvements. *Scr. Mater.* **2005**, *52*, 963−968.

DOI: 10.1021/acs.jpcc.8b02258
J. Phys. Chem. C XXXX, XXX, XXX−XXX